Second-Harmonic Generation from Hyperbolic Plasmonic Nanorod Metamaterial Slab

Giuseppe Marino, Paulina Segovia, Alexey V. Krasavin, Pavel Ginzburg, Nicolas Olivier, Gregory A. Wurtz, and Anatoly V. Zayats*

Hyperbolic plasmonic metamaterials provide numerous opportunities for designing unusual linear and nonlinear optical properties. In this work, second-harmonic generation in a hyperbolic metamaterial due to a free-electron nonlinear response of a plasmonic component of the metamaterial is studied. It is shown that owing to a rich modal structure of an anisotropic plasmonic metamaterial slab, the overlap of fundamental and second-harmonic modes results in the broadband enhancement of radiated second-harmonic intensity by up to 2 orders of magnitude for TM- and TE-polarized fundamental light, compared to a smooth Au film under TM-polarised illumination. Compared to the radiated second-harmonic intensity from a bulk $LiNbO_3$ nonlinear crystal of the same thickness, the SHG intensity from a metamaterial slab may be up to 2 orders of magnitude higher at the certain metamaterial resonances. The results open up possibilities to design tuneable frequency-doubling integratable metamaterial with the goal to overcome limitations associated with classical phase matching conditions in thick nonlinear crystals.

1. Introduction

Second-harmonic generation (SHG) is used frequently in modern laser technologies and photonic applications.[1] The main advantage of this frequency doubling technique is the possibility of coherent light generation at the wavelengths complementary to typical radiative decay channels of a gain medium and metrology of ultrashort pulses.[2] SHG implementations based on nonlinear optical crystals are significantly constrained by phase matching conditions: fundamental and second-harmonic waves are required to propagate in phase to obtain optimum nonlinear energy conversion.[1] The operational bandwidth for ultrashort pulses is another limitation for frequency conversion in bulk nonlinear crystals.[3]

To overcome these limitations and increase integrability of nonlinear optical components, various nonlinear nanostructured media have been proposed for second-harmonic (SH) generation based on nanoparticles, optical nanoantennas, and metamaterials.[4–7] These approaches use the light confinement and enhancement in plasmonic (metallic) nanostructures to locally increase the fundamental field strength upon which SHG depends quadratically.[1] In multi-resonant structures, SHG effect can be further enhanced with the additional resonant scattering provided by the nanostructure at the SH frequency.[1,8,9] Thus, conventional phase matching conditions can be replaced with a modal overlap at the fundamental and SH frequencies in the nanostructures.[4–7] In order to realise these conditions experimentally, diverse geometries have been used such as a broadband optical nanoantennas,[6] a composite nanoparticle made of a rod and a V-shaped nanoantenna,[5] nanoscale spirals,[10] and split-ring resonator based metamaterials.[7]

In another approach to achieve broadband and alignment-free phase-matching, the so-called ε-near-zero (ENZ) metamaterials were proposed which by their nature achieve phase-matching conditions due to the electrostatic character of the second-harmonic field inside the medium.[11] They however operate only in a finite frequency range where the ENZ occurs, near the effective plasma frequency of a metamaterial.[12] Anisotropic ENZ metamaterials also typically possess broadband hyperbolic and elliptic dispersions allowing a rich structure of the supported modes, including low and negative group velocity modes[12,13]

Dr. G. Marino, Dr. P. Segovia, Dr. A. V. Krasavin, Dr. P. Ginzburg, Dr. N. Olivier, Dr. G. A. Wurtz, Prof. A. V. Zayats
Department of Physics
King's College London
Strand, London, WC2R 2LS, United Kingdom
E-mail: giuseppe.marino@univ-paris-diderot.fr

Dr. G. Marino
Matériaux et Phénomènes Quantiques
Université Paris Diderot-CNRS
Paris, 75013, France

Dr. P. Segovia
Departamento de Óptica
CICESE
Ensenada, B.C. México

Dr. P. Ginzburg
Department of Electrical Engineering
Tel Aviv University
Ramat Aviv 69978, Israel

Dr. N. Olivier
Department of Physics and Astronomy
The University of Sheffield
Sheffield, S10 2TN, United Kingdom

Dr. G. A. Wurtz
Department of Physics
University of North Florida
Jacksonville, FL 32224, USA

The ORCID identification number(s) for the author(s) of this article can be found under https://doi.org/10.1002/lpor.201700189

DOI: 10.1002/lpor.201700189

which may be favourable for SHG enhancement. Such metamaterials can be realised on a macroscopic scale using arrays of aligned plasmonic nanorods so that the mode structure of the metamaterial can be efficiently tuned by changing the nanorod array geometrical parameters. In particular, Au nanorod based metamaterials provide tuneable ENZ behaviour throughout both the visible and near infrared spectral ranges via adjustment of structural parameters.[14] While the centrosymmetric crystal lattice of gold, limits the source of the second-order nonlinearity to the surface nonlinear contributions, the nanostructured geometry of the Au nanorod metamaterial may exploit a large surface area with high field confinement to provide efficient second-harmonic generation. Due to the fact that this internal structure of the metamaterial and the local fields inside the metamaterial[15,16] are paramount for the description and understanding of SHG processes, the effective medium approximation for the metamaterial description is not applicable for modelling SHG processes and full-vectorial, microscopic considerations should be employed.

In this paper, we study intrinsic second-harmonic generation processes in plasmonic nanorod metamaterial slabs and show its enhancement at multiple resonant wavelengths determined by the mode structure of the metamaterial at both fundamental and second-harmonic frequencies. The perturbative hydrodynamic approach for Au nonlinearity description in a broad spectral range has been used and microscopic numerical simulations of the near-field and radiated SHG from a metamaterial slab have been performed in both reflection and transmission. It is shown that both transverse electric (TE) and transverse magnetic (TM) modes of the planar waveguide formed by a metamaterial slab provide efficient SHG tuneable over the entire visible region of the spectrum in both reflection and transmission, thus allowing efficient SHG for both polarizations of the fundamental light. The SHG enhancement by several orders of magnitude is observed when a modal overlap between the fundamental and second harmonic frequencies takes place, emulating the so-called double-resonant conditions.[4,17,18] By designing such plasmonic nanorod metamaterials, the enhancement of frequency doubling efficiency can be achieved in a desired wavelength range, in the same way as third-order nonlinearity has been designed,[19] or similar to frequency-doubling phase-matched meta-reflectors in the THz spectral range.[20,21] This further enables nanoscale optical tomography via optimisation of the far-field second-harmonic radiation patterns of a nano-objects embedded in a hyperbolic metamaterial slab antenna.[22]

2. Modelling Approach

2.1. Metamaterial Slab Properties

The metamaterial studied here is formed by an assembly of aligned metallic (Au) nanorods (12 nm radius, 300 nm length and 60 nm period of a square lattice) hosted in an alumina matrix (**Figure 1**). The optical properties of this uniaxial metamaterial can be inferred from the local effective medium theory (EMT)[23] via the diagonal effective permittivity tensor of the form $\hat{\varepsilon}^{eff} = [\varepsilon_x^{eff}, \varepsilon_y^{eff} = \varepsilon_x^{eff}, \varepsilon_z^{eff}]$ (Figure 1). A TE-polarized incident light with the electric field normal to the nanorod axis always experiences positive effective permittivity $\varepsilon_{x,y}^{eff}$. In contrast, a TM polarized incident light, having an electric field components both along and normal to the nanorod axis will be governed by the effective permittivity components $\varepsilon_{x,y}^{eff}$ and ε_z^{eff}. In the former case, the metamaterial behaves as a dielectric over the entire spectral range investigated, while in the latter, the optical response of the metamaterial transitions from an anisotropic dielectric behaviour ($\varepsilon_{x,y}^{eff}, \varepsilon_z^{eff} > 0$, elliptic dispersion) to a plasmonic-like behaviour ($\varepsilon_{x,y}^{eff} > 0$, $\varepsilon_z^{eff} < 0$, hyperbolic dispersion) passing through the ENZ wavelength range at around a wavelength of 710 nm at which $\mathcal{R}e(\varepsilon_z^{eff}) = 0$, determining the effective plasma frequency of metamaterial.[12] In the case of a relatively low material losses, the optical properties of this type of metamaterials may also be influenced by the presence of a second TM polarised wave associated with the spatial dispersion of a composite medium,[13,16] further enriching the spectrum of supported waveguided modes.[25]

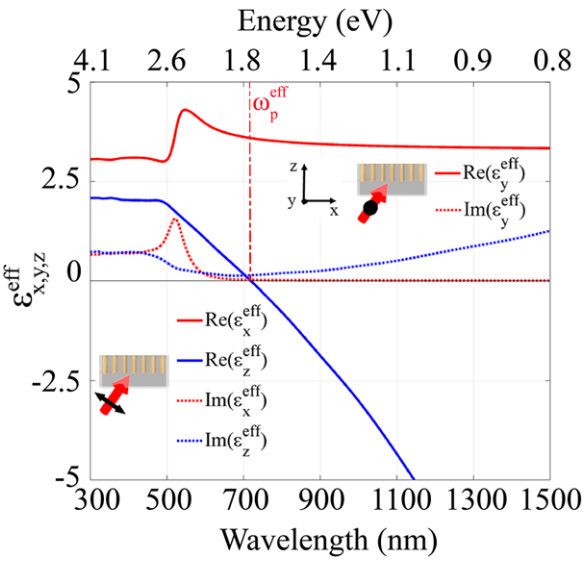

Figure 1. Effective permittivity of the anisotropic nanorod metamaterial based on a square array of Au nanorods (12 nm radius, 300 nm length and 60 nm period) embedded in alumina (n = 1.6). Au permittivity has been taken from Ref. [24].

The anisotropic metamaterial slab placed on a glass substrate supports a set of TE and TM modes (**Figure 2**a and b). For incident angles lying within the light cone in air, these modes are the cavity modes of the planar slab of the metamaterial. For larger angles, the modes are accessible with the illumination through the substrate and are leaky waveguided mode of the metamaterial slab.[12] In the frequency range above the effective plasma frequency of the metamaterial, both TE and TM modes are typical modes of the anisotropic planar waveguide, if nonlocal effects are not important; below it, the metamaterial supports bulk plasmon polaritons,[12] and the TM modes may have positive, vanishingly small or negative group velocity. TE modes always behave as modes of an anisotropic dielectric slab.

The EMT can reasonably well predict linear far-field optical response, however it cannot describe local near-fields in the vicinity or inside the nanorod array,[15] which are responsible for SHG. For this reason, in this work the use of the EMT is limited to

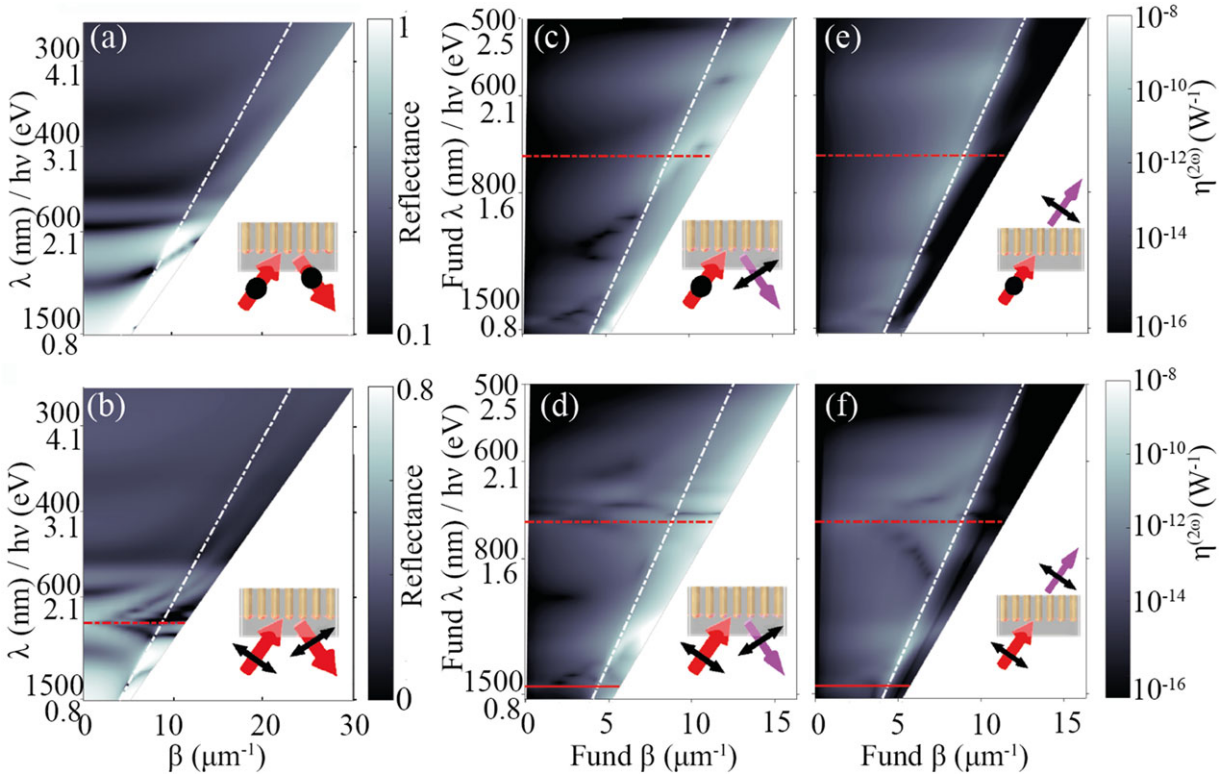

Figure 2. a),b) Reflectance dispersion of the metamaterial slab as in Figure 1 for a) TE and b) TM polarisations. c)–f) The spectra of the radiated (far-field) SH intensity for different angles of incidence of the fundamental light: c),d) reflected and e),f) transmitted SHG signal for c),e) TE-polarised and d),f) TM-polarised fundamental light. SHG is always TM-polarised. The effective plasma frequency of the metamaterial at the fundamental and SH wavelengths, obtained from the EMT,[23] is shown with the horizontal dashed and solid lines, respectively. The light line in air is shown with a white dashed line. Low SHG intensity near the normal incidence excitation is related to the symmetry consideration of far-field SHG. Transmitted SH light is generated even under the excitation in the total-internal reflection configuration due to the presence of the metamaterial slab modes (Fabry-Perot type) at the SH wavelength coupled to light in a superstrate (air). The SHG model used for the simulations (Equation (1)) considers only the free-electron contribution to the second-order nonlinear susceptibility and is valid for the frequencies away from the interband transitions in Au (photon energies smaller than approximately 2.5 eV).

model the linear response at both fundamental and SH frequencies, while full-wave numerical simulations are used for the SHG simulations: the microscopic sources calculated from the full-wave solutions of the linear fields are necessary for a correct description of the SHG.

2.2. Modelling Second-Order Nonlinearity of Au Nanorods

Nonlinear polarization related to conduction electrons of noble metals, such as gold and silver, is well described by the hydrodynamic model.[26] The latter holds only for the spectral range well below the plasma frequency away from the interband transitions and Coulomb collisions, occurring at high and low frequencies, respectively. Following Refs. [27–29], the contribution of both conduction and bound electrons can be included in the model via a complex permittivity at both fundamental and SH frequencies, while retaining only a free-electron contribution to the nonlinear polarization.

Let us consider the classical hydrodynamic equation for conduction electrons: $m^*\frac{d\boldsymbol{v}}{dt} + m^*\boldsymbol{v}\cdot\nabla\boldsymbol{v} = -e\boldsymbol{E} - \gamma_0 m^*\boldsymbol{v} - e\mu_0\boldsymbol{v}\wedge\boldsymbol{H}$, where $\boldsymbol{v}(\boldsymbol{r},t) = \boldsymbol{j}(\boldsymbol{r},t)/en(\boldsymbol{r},t)$ is the electron velocity with $\boldsymbol{j}(\boldsymbol{r},t)$ and $n(\boldsymbol{r},t)$ being the electron current density and electron density, respectively. The equation includes a convective term accounting for the acceleration of charges, a linear term in the charge density, a viscosity term containing the damping frequency γ_0 of conduction electrons and, finally, the Lorentz-force term. Nevertheless, additional terms such us quantum pressure of electron gas, which may become important for metallic nanostructures of smaller sizes,[10] are not taken into account in this model.[28] Given the continuity equation: $\dot{n}(\boldsymbol{r},t) = -(\nabla\cdot\boldsymbol{j})/e$, where $\boldsymbol{j} = \dot{\boldsymbol{P}}$, the hydrodynamic equation can be written in terms of the polarization $\boldsymbol{P}$. Thus, adopting a perturbative methodology in the undepleted pump approximation (the non-perturbative approach is described in Ref. [30]), one can use the frequency domain approach to obtain the polarization at the SH frequency, $\boldsymbol{P}^{(2\omega)}$, as a function of the fundamental field by collecting terms up to the second order: $\boldsymbol{P}_S^{(2\omega)} = 4\pi\varepsilon_0\{\beta\boldsymbol{E}^{(\omega)}\nabla\cdot[\chi_D^{(\omega)}\boldsymbol{E}^{(\omega)}] + \frac{{\omega_p}^2}{\omega^2}\frac{\beta}{4}\nabla[\boldsymbol{E}^{(\omega)}\cdot\boldsymbol{E}^{(\omega)}]\}$, where $\beta = \frac{e}{8\pi m^*\omega^2}[\frac{\omega^2}{{\omega_p}^2}]\chi_D^{(\omega)}[\frac{(2\omega)^2}{{\omega_p}^2}]\chi_D^{(2\omega)}$, $\chi_D^{(\omega)} = \varepsilon_D^{(\omega)} - 1 = -\frac{{\omega_p}^2}{\omega^2+i\gamma_0\omega}$ is the Drude susceptibility, ω_p is the plasma frequency of a metal, e and m^* are the electron charge and effective mass, respectively, and γ_0 is the Drude damping. The parameter β accounts for electron losses in the conduction band at both the fundamental and SH frequencies via $\chi_D^{(\omega)}$ and $\chi_D^{(2\omega)}$, respectively. The first term in the

nonlinear polarization, accounting for a dot product between the electric field and its divergence, is the quadrupole-like Coulomb term, while the second term accounting for the gradient of the square of the electric field is produced by convective and Lorentz forces. These terms have a δ-function-like behaviour at the metal surface, thus the bulk contribution to second-order response can be neglected. It is interesting to note that in the limit of a free-electron gas when $\beta = \frac{e}{8\pi m^* \omega^2}$, the above polarization takes the form reported in Ref. [26]. Finally, due to the continuity of the electric displacement across the metal surface, we can write the electric field as a function of the spatially varying complex permittivity of a metal, ε_r, considering both intraband and interband transitions in the linear polarization, but only free-electron contribution to nonlinear response. Thus, by defining a local coordinate system at each point of the nanorod surface with unit vectors $\hat{\boldsymbol{Z}}$ and $\hat{\boldsymbol{X}}$ orthogonal and tangential to the surface, respectively, we can write the current density at the nanorod surface, $\boldsymbol{j}_S^{(2\omega)}$, in terms of its local tangential and orthogonal components:

$$\begin{cases} \hat{\boldsymbol{Z}} \cdot \boldsymbol{j}_S^{(2\omega)} = -2i\omega\varepsilon_0\alpha\chi_D^{(2\omega)}\left(\chi_D^{(\omega)}\right)^2 \left[(\varepsilon_r + 3)/4\right] \boldsymbol{E}_{S,\hat{\boldsymbol{Z}}}^{(\omega)} \boldsymbol{E}_{S,\hat{\boldsymbol{Z}}}^{(\omega)} \\ \hat{\boldsymbol{X}} \cdot \boldsymbol{j}_S^{(2\omega)} = -2i\omega\varepsilon_0\alpha\chi_D^{(2\omega)}\left(\chi_D^{(\omega)}\right)^2 \boldsymbol{E}_{S,\hat{\boldsymbol{X}}}^{(\omega)} \boldsymbol{E}_{S,\hat{\boldsymbol{Z}}}^{(\omega)} \end{cases} \quad (1)$$

where $\alpha = \frac{2e\omega^2}{m^* {\omega_p}^4}$. It should be noted that the proportionality between the current density and the electric field contains the susceptibility at the fundamental frequency taken twice and the susceptibility at the SH frequency, as expected for a three-wave interaction. The tangential term is derived only from the quadrupole-like Coulomb term of the nonlinear polarization equation. At the same time, the orthogonal term has, in addition, contributions from the convective and Lorentz forces terms of the nonlinear polarization equation. As a result, the former is continuous at the surface, while the latter shows a surface discontinuity. From this consideration, one can see that the orthogonal term, $\hat{\boldsymbol{Z}} \cdot \boldsymbol{j}_S^{(2\omega)}$ is dominant, which is in agreement with previously reported results.[31,32] Only the orthogonal term is considered thereafter. Finally, it is important to underline that in the model above, only the free-electron contribution to the nonlinear response is taken into account and the model is valid for the photon energies smaller than approximately 2.5 eV, where the interband transitions in Au are less important.

2.3. Numerical Modelling

For the numerical simulations of the SHG emitted by the metamaterial, we used a frequency-domain finite element solver (Comsol Multiphysics), in the framework of the undepleted pump approximation described above. The model uses the Floquet boundary conditions for a metamaterial square unit cell to mimic a planar infinite slab. Rounded tips of the nanorods have been considered to avoid the computational complexity associated with sharp edges. The rounding procedure consists of a geometry with two hemispheres placed at the top and bottom of each cylinder, having the same radius as the cylinder. The total height of the meta-atom is $H_{\mathrm{cyl}} + 2r = 300$ nm where H_{cyl} and r are height and radius of the cylinder, respectively. The nonlinear source was calculated by taking the electric field just inside the metal and place the polarization sheet just outside.[31] The model has also been tested on Au nanoparticles such as nanospheres and nanoprisms leading to a SH emission in agreement with Ref. [33].

3. Metamaterial Slab Modes and Near-Field SHG

Angular and spectral dependences of reflected and transmitted far-field SHG excited by TE and TM polarized fundamental light exhibit a complex structure of the enhanced and supressed SHG (Figure 2c-f). The generated SH light is always TM-polarized. Considering both linear reflectance and SH spectra either for TE (Figure 2a, c and e) or TM incident polarization (Figure 2b, d and f), it becomes clear that the slab modes are responsible for the enhancement of the observed SHG. While for the far-field radiated SHG, the integration over the SHG propagation direction smears out the contribution of individual modes, the analyses of the near-field SHG intensities allows one to unambiguously identify the role of TM and TE modes of the metamaterial slab (**Figure 3**a and b).

The individual modes supported by the metamaterial slab were identified (Figure 3a and b) by comparing the numerically calculated dispersion to the analytically evaluated mode structure in the framework of the EMT.[12] A good agreement between the simulated and analytical modes allows to label the observed modes corresponding to the minima in the reflection dispersion. For TE polarisation, a set of modes of the anisotropic dielectric slab can be identified (denoted with En, where n is the mode index) in the dispersion plot (Figure 3a). For TM polarisation, bulk plasmon polaritons are supported by the metamaterial slab (these modes denoted with hn) at the frequencies below the effective plasma frequency (Figure 3b), while modes at higher frequencies correspond to the modes of a conventional elliptic-dispersion dielectric slab (denoted as en). One can observe the presence of the numerically calculated modes occurring above the effective plasma frequency (Figure 3b) with hyperbolic-like behaviour which are related to the nonlocal response, not described by the EMT.[13]

The analysis of the near-field SHG spectra allows one to identify the SHG enhancement at the positions of the modes of the metamaterial slab at either fundamental or SH frequencies (Figure 3d and f). The strongest SHG enhancement corresponds however to an overlap of the modes at the fundamental and second-harmonic frequencies. The spectral features of the far-field (Figure 2c and d) and near-field (Figure 3d and f) SH spectra are the same with maxima corresponding to the modes of the metamaterial slab. The metamaterial slab modes identified in the SHG spectral dependencies (red labels for either elliptic or hyperbolic modes at the fundamental frequency, green labels for hyperbolic SHG modes, due to the TM polarisation of the generated SH light), unambiguously show the correspondence of the mode position and the SHG enhancement in the single-resonant (when either the fundamental or SH light is coupled to the mode) and especially double-resonant (when both the fundamental and SH light is coupled to the slab modes) conditions. For angles of incidence of 30° and 48° and TE polarization (Figure 3d), the double-resonant conditions for TE modes occur

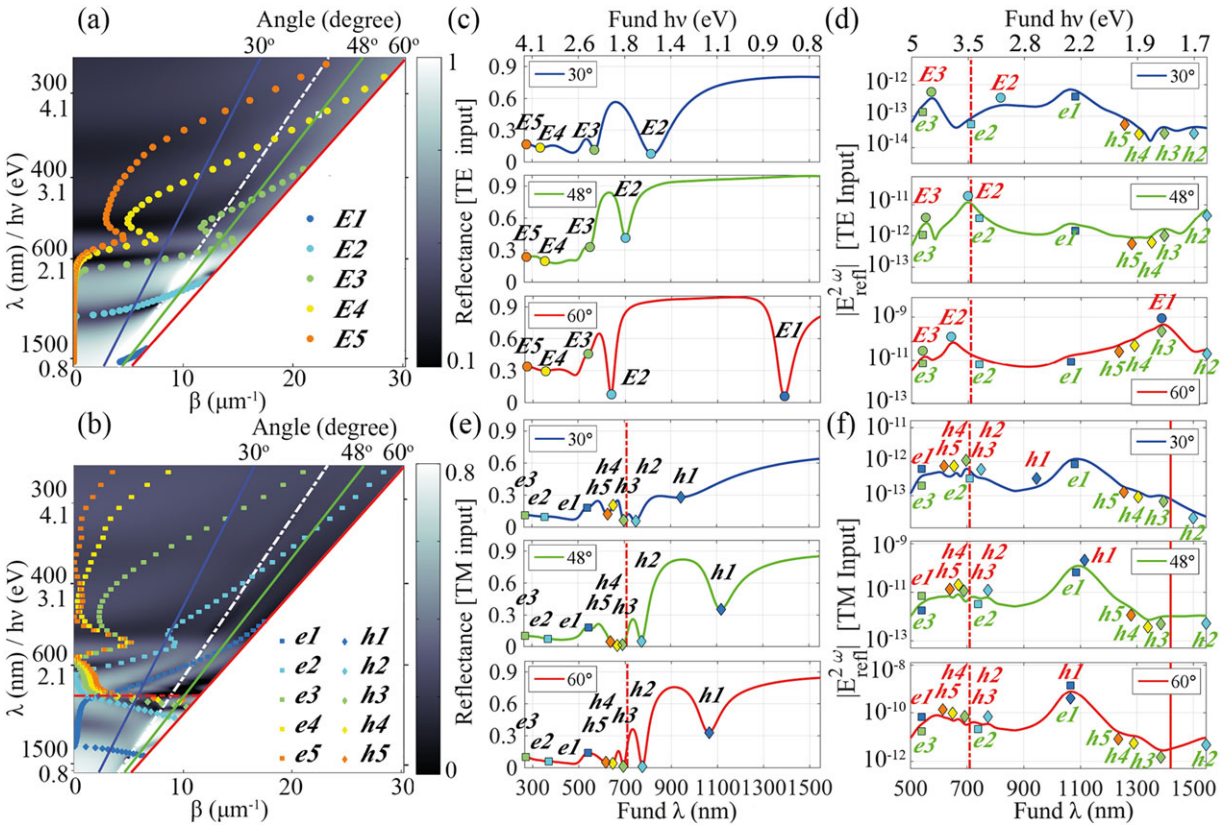

Figure 3. a) TE and b) TM reflectance dispersions of the metamaterial slab overlaid with the analytically simulated mode structure. The effective bulk plasma frequency of the metamaterial is shown with a horizontal line. c) TE and e) TM reflectance spectra for selected wavelengths with mode identification: En modes refer to modes allowed for ordinary polarization, en and hn modes refer to modes allowed in the elliptical and hyperbolic regimes, respectively, for extraordinary polarization. d),f) Spectra of the near-field SHG measured 5 nm below the metamaterial in a glass substrate for d) TE and f) TM polarization of the fundamental light. SH light is TM polarized irrespectively of the fundamental light polarization. Red and green labels identify modes at the fundamental and second-harmonic frequencies, respectively. The effective plasma frequency of the metamaterial at the fundamental and SH wavelengths is shown with the vertical dashed and solid lines, respectively.

primarily for the SHG in the short-wavelength spectral range; e.g., the highest SHG efficiency is observed at 2.3 eV and 1.77 eV, respectively. High efficiency can be achieved for TM modes in the NIR spectral range for a broader range of incident angles (Figure 3f) due to the involvement of bulk plasmon-polaritons in the hyperbolic spectral range with almost flat dispersion; e.g., at 1.16 eV excitation, where the hyperbolic h1 mode at the fundamental frequency overlaps with the E1 mode at the SH frequency. Thus, strong SHG enhancement can be observed at multiple "double-resonant" wavelengths allowing for efficient SH generation at multiple wavelength with the same metamaterial slab.

The field confinement near the nanorods forming the metamaterial, associated with the excitation of different modes was simulated and can be seen from the plotted polarisation distributions: the stronger field enhancement the higher the induced SH polarization. For example, one can observe that the mode h1 at 1.16 eV (**Figure 4**d) yields the highest field confinement in the proximity of the reflection interface of the metamaterial slab, followed by the mode E1 at 0.89 eV (Figure 4a). In addition to the mode spectral position, an overlap integral between the microscopic polarizations at the fundamental and SH frequencies is important to observe efficient SHG enhancement.[7] For example, the mode e1 (Figure 4e) exhibits highest field confinement in the proximity of the interface of the metamaterial slab, followed by the mode h3 (Figure 4b). The orthogonal to the surface components of both the nonlinear polarization $\chi^{(2\omega)}_{\perp\perp\perp} \mathrm{E}^{(\omega)}_{\perp}(\vec{r},\omega)\mathrm{E}^{(\omega)}_{\perp}(\vec{r},\omega)$ and the SH field distribution $\mathrm{E}^{(\omega)}_{\perp}(\vec{r},2\omega)$, together with their complex scalar product describing both the overlap and phase relations

$$\chi^{(2\omega)}_{\perp\perp\perp} \mathrm{E}^{(\omega)}_{\perp}(\vec{r},\omega)\, \mathrm{E}^{(\omega)}_{\perp}(\vec{r},\omega)\, \overline{\mathrm{E}^{(\omega)}_{\perp}(\vec{r},2\omega)} \tag{2}$$

are plotted for the selected modes and both fundamental light polarizations in **Figure 5**. The corresponding values of the relative overlap, i.e., the magnitude of the vector sum over the nanorod surface of the miscroscopic nonlinear sources in Equation (2), are equal to approximately 2.6×10^{-10} and 3.1×10^{-10} for the modes E1-h3 at 0.89 eV and h1-e1 at 1.16 eV, respectively. For comparison, for the off-resonant excitation at 0.4 eV, the relative overlap integral values are much smaller being 1×10^{-12} for both TE and TM fundamental light.

Interestingly, the relative overlap near the reflection interface for the modes E1-h3 and h1-e1 are similar while the resulting

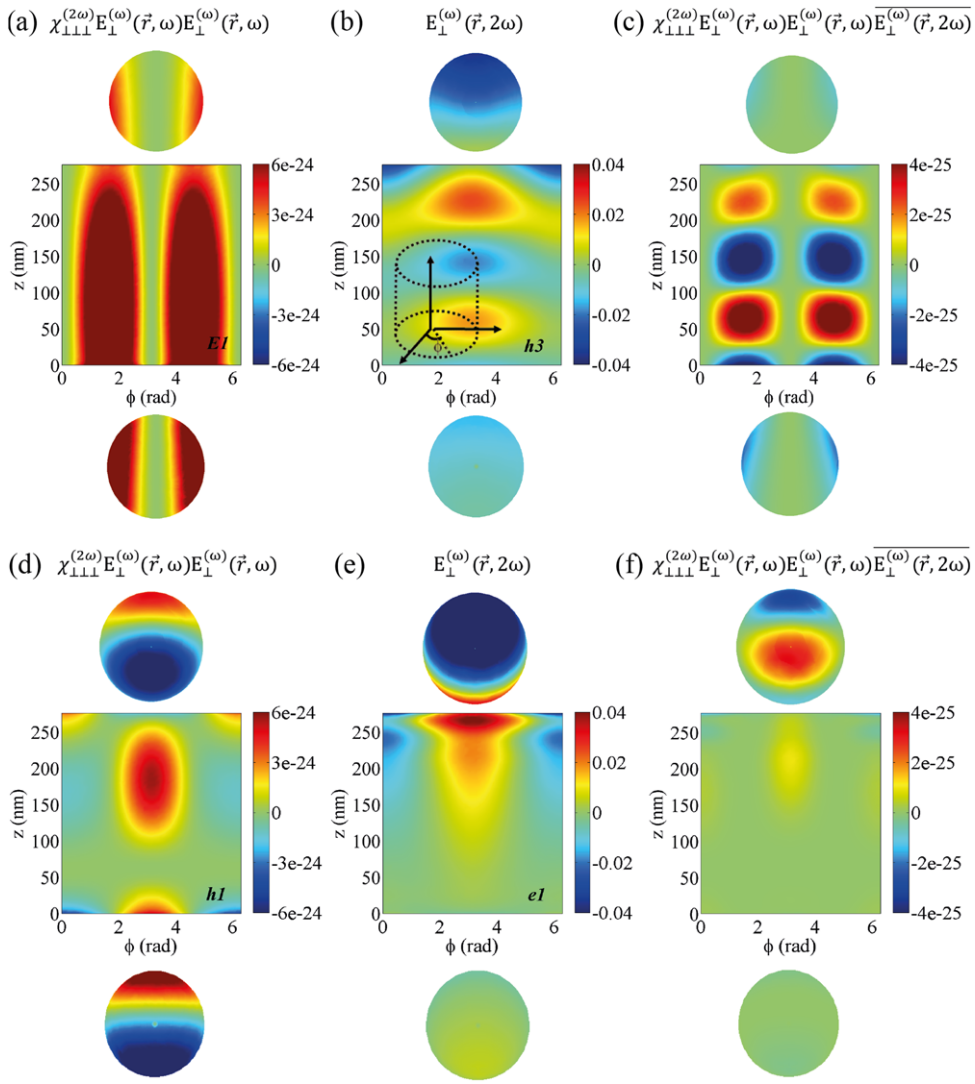

Figure 4. Nonlinear polarization, fields and their overlaps on the surface of the nanorod in cylindrical co-ordinates (as shown in the insert in b). a),d) Orthogonal to the nanorod surface (P_n) component of the nonlinear polarization (real part) for a) E1 and d) h1 modes induced by the TE and TM polarized fundamental light at 0.89 eV and 1.16 eV, respectively. b),e) The electric field distributions (real part) of the h3 and e1 modes at the SH frequency (1.78 and 2.32 eV, respectively). c),f) Overlap (real part) between c) E1 and h3 modes and f) h1 and e1 modes. Fundamental light is incident from the top at the angle of 60°.

reflected SHG intensities are significantly different with the intensity for the modes E1-h3 being three times higher (Figure 2c and d). This highlights the importance of additional considerations of the mode properties. Firstly, both the high field enhancement at the fundamental frequency in the proximity of the interface of the metamaterial slab and high second-order susceptibility of Au for the fundamental light in the infrared spectral region favor the respective modes for achieving strong reflected SHG. Secondly, a strong field enhancement at the SH frequency near the interface, corresponding to the slab modes, also enhances the near-field and radiated SH. Not only the symmetry of the fundamental and SH field distributions are important to achieve a significant overlap of the resonant fields, but also the local overlap near the interface, responsible for the radiation of SH light.

4. Radiated SH Spectra from the Metamaterial Slab

Both reflected and transmitted far-field SHG have comparable intensities with the spectral dependences determined by the mode structure of the slab (Figure 2c, d, e and f). In order to compare this nonlinear metamaterial performance with other nonlinear platforms, a SH conversion efficiency is defined in a usual way as $\eta^{(2\omega)} = I^{(2\omega)}/(I^{(\omega)})^2$, where $I^{(2\omega)}$ and $I^{(\omega)}$ are the average intensities of the radiated SH and incident fundamental fields. A maximum conversion efficiency in the reflected far-field SHG of about 2×10^{-7} W^{-1} is achieved under the TM polarized fundamental light excitation at 1.16 eV at an incident angle of 60° in the substrate; this is approximately 4 orders of magnitude higher than for the TE polarized light at the same conditions. Interestingly, for the same illumination conditions, at a fundamental frequency

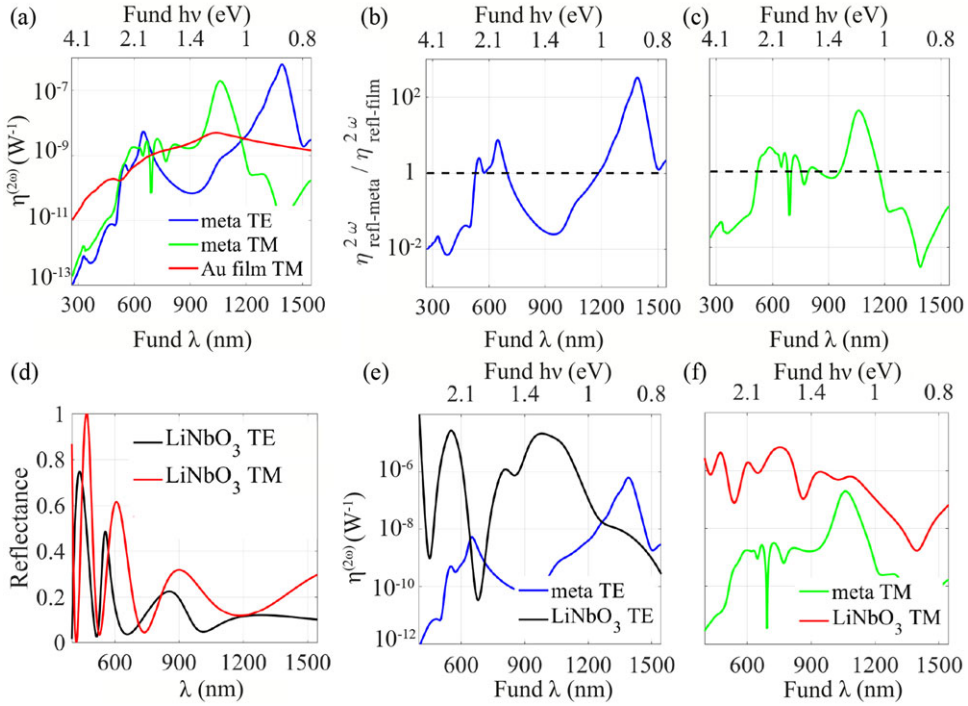

Figure 5. a) Far-field reflected SH spectra from a smooth Au surface (red line) and the nanorod metamaterial (extracted from Figure 2c and d) for TE-polarised (blue line) and TM-polarised (green line) fundamental light. b),c) The ratio of the SHG intensities reflected from the metamaterial for b) TM- and c) TE-polarised excitation and a smooth Au surface for TM-polarised excitation. A dashed black line indicates a ratio equal 1. d) Linear reflectance and e),f) comparison of the reflected SH spectra for TE e) and TM f) fundamental light from a 300 nm thick $LiNbO_3$ crystal and the metamaterial slab. The $LiNbO_3$ permittivity has been taken from Ref. [40] and the bulk nonlinearities for a trigonal crystal of class 3m with d_{22}, d_{31} and d_{33} nonzero susceptibility components are taken from Ref. [41]. The angle of incidence is 60° in all cases.

of 0.89 eV, the TE-polarized excitation (conversion efficiency 6×10^{-7} W^{-1}) provides almost 5 orders of magnitudes higher SHG than TM-polarized light. This strong wavelength and angular dependences are a direct consequence of the mode structure of the metamaterial slab and the internal structure of the nanorod metamaterial, providing both significant field enhancement at the mode frequencies[15] and large surface area (approximately 7 times larger than for a smooth Au film). The internal structure of the metamaterial composite generally favours the TE-mode excitation which has a strong electric field component normal to the nanorod surface. These counterintuitive polarization properties are similar to those observed in other metamaterials with strong internal local fields.[34]

In order to benchmark the observed SHG intensities from the metamaterial, the reflected-SHG spectrum excited with TM-polarized fundamental light from a smooth Au surface has been calculated using the same model for Au nonlinearity (Figure 5a). The SHG from a smooth film has a featureless wavelength dependence with a dip at around 2.5 eV related to the interband transitions in Au at the fundamental frequency.[35] A comparison with the metamaterial SHG intensities for TE and TM excitations at an angle of incidence of 60° shows that the metamaterial outperforms the Au film in the resonant conditions by approximately two orders of magnitudes (Figure 5a, b and c). The polarisation properties of this SHG are different from a smooth Au film for which the SHG excited with the TM-polarised light is always dominant.

For different angles of incidence, there is a redistribution of the peak intensities in the SHG spectra according to the dispersion of the involved modes of the metamaterial slab, but the maximum enhancement measured with respect to the smooth film remains in the same range. Moreover, strong radiated SHG is also observed in transmission even for the excitation under total internal reflection (TIR) conditions as the dispersion of the metamaterial slab has the modes at the SH frequencies outside TIR range (Figure 2e and f). Please note that under the excitation at normal incidence, low SHG intensities are observed for all polarisation configurations (Figure 2c, d, e and f). due to the symmetry breaking requirements for far-field SHG[36,37] (these requirements are not applicable in the near-field region[38]). Similarly, for a smooth Au film under the illumination at normal incidence, the simulated SHG is vanishingly small, within numerical noise, as expected from symmetry considerations.

In order to further benchmark the observed SHG from metamaterials, the reflected-SHG spectrum from the metamaterial has been compared to the SHG from a bulk nonlinear crystal $LiNbO_3$ (Figure 5d, e and f), with the same thickness as the metamaterial slab. Calculations are done following the same full 3D vectorial model used for the metamaterial and considering bulk nonlinear sources for $LiNbO_3$.[39] Reflectance from the thin film of $LiNbO_3$ (Figure 5d) has the characteristic spectrum determined by the thin film interference.[42] Here, the angle of incidence is above the critical angle of total internal reflection for waveguided modes in the dielectric slab. As a consequence,

the reflected-SHG spectrum from this nonlinear waveguide (Figure 5e and f) is enhanced in correspondence with the modal structure at both fundamental and SH frequencies, outperforming the SHG from Au metamaterial for TM-polarized excitation (Figure 5f). For TE-polarized fundamental light in the near infrared spectral range, the SHG from the metamaterial can be up to 2 orders of magnitude, in correspondence to the nonlinear resonance at a fundamental frequency of 0.89 eV (Figure 5e).

5. Conclusions

We have numerically studied SHG from an anisotropic hyperbolic metamaterial in different polarisation configurations and for different angles of incidence. We have adopted a perturbative, nondepleted pump approximation of the SHG description with hydrodynamic nonlinearity of Au nanorod meta-atoms forming the metamaterial and also taken into account the internal structure of the metamaterial composite. The simulations show strongly enhanced reflected SHG when both fundamental and generated light is coupled to the modes of the metamaterial slab and confined in the proximity of the reflection interface, which is facilitated by the modes dispersion in the hyperbolic regime. Due to a rich spectrum of the modes supported by the hyperbolic anisotropic slab waveguide, the enhanced SHG can be observed in a broad spectral range. Due to the internal structure of the metamaterial composite, the polarisation properties of the SHG are different from conventional smooth metal film, and TE-mode excitation with the strong component normal to the nanorod surface may dominate over TM-polarised excitation. By designing the plasmonic nanorod metamaterials, the enhancement of frequency doubling efficiency can be achieved in a desired wavelength range by controlling the modal structure of the metamaterial slab.

Acknowledgment

This work was supported, in part, by EPSRC (UK), the ERC iPLASMM project (321268), and US Army Research Office (W911NF-12-1-0533). A.Z. acknowledges support from the Royal Society and the Wolfson Foundation. The data access statement: all data supporting this research are provided in full in the results section.

Conflict of Interest

The authors declare no conflict of interest.

Keywords

hyperbolic metamaterials, plasmonics, second harmonic generation

Received: July 15, 2017
Revised: November 30, 2017
Published online: January 15, 2018

[1] R. W. Boyd, *Nonlinear Optics*, San Diego, USA: Academic Press, **2008**.
[2] R. Holzwarth, Th. Udem, T. W. Hänsch, J. C. Knight, W. J. Wadsworth, P. St. J. Russell, *Phys. Rev. Lett.* **2000**, *85*, 2264.
[3] C. Rulliere, *Femtosecond Laser Pulses*, New York, NY: Springer, **2005**.
[4] P. Ginzburg, A. Krasavin, Y. Sonnefraud, A. Murphy, R. J. Pollard, S. A. Maier, A. V. Zayats, *Phys. Rev. B* **2012**, *86*, 085422.
[5] M. Celebrano, X. Wu, M. Baselli, S. Großmann, P. Biagioni, A. Locatelli, C. De Angelis, G. Cerullo, R. Osellame, B. Hecht, L. Duò, F. Ciccacci, M. Finazzi, *Nat. Nanotechnol.* **2015**, *10*, 412.
[6] H. Aouani, M. Rahmani, M. Navarro-Cía, S. A. Maier, *Nat. Nanotechnol.* **2014**, *9*, 290.
[7] K. O'Brien, H. Suchowski, J. Rho, A. Salandrino, B. Kante, X. Yin, X. Zhang, *Nat. Mater.* **2015**, *14*, 379.
[8] A. V. Zayats, V. Sandoghdar, *Opt. Comm.* **2000**, *178*, 245.
[9] A. Zayats, V. Sandoghdar, *J. Microsc.* **2001**, *202*, 94.
[10] A. Krasavin, P. Ginzburg, G. A. Wurtz, A. V. Zayats, *Nat. Comm.* **2016**, *7*, 11497.
[11] M. A. Vincenti, S. Campione, D. de Ceglia, F. Capolino, M. Scalora, *New J. Phys.* **2012**, *14*, 103016.
[12] N. Vasilantonakis, M. E. Nasir, W. Dickson, G. A. Wurtz, A. V. Zayats, *Laser Photon Rev.* **2015**, *9*, 345.
[13] P. Ginzburg, D. J. Roth, M. E. Nasir, P. Segovia, A. V. Krasavin, J. Levitt, L. M. Hirvonen, B. Wells, K. Suhling, D. Richards, V. A. Podolskiy, A. V. Zayats, *Light: Sci. Appl.* **2017**, *6*, e16273.
[14] M. Nasir, S. Peruch, N. Vasilantonakis, W. P. Wardley, W. Dickson, G. A. Wurtz, A. V. Zayats, *Appl. Phys. Lett.* **2015**, *107*, 121110.
[15] K.-T. Tsai, G. A. Wurtz, J.-Y. Chu, T.-Y. Cheng, H.-H. Wang, A. V. Krasavin, J.-H. He, B. M. Wells, V. A. Podolskiy, J.-K. Wang, Y.-L. Wang, A. V. Zayats, *Nano Lett.* **2014**, *14*, 4971.
[16] B. M. Wells, A. V. Zayats, V. A. Podolskiy, *Phys. Rev. B* **2014**, *89*, 035111.
[17] A. Hayat, M. Orenstein, *Opt. Lett.* **2007**, *32*, 2864.
[18] D. de Ceglia, M. A. Vincenti, C. De Angelis, A. Locatelli, J. W. Haus, M. Scalora, *Opt. Exp.* **2015**, *23*, 1715.
[19] A. D. Neira, N. Olivier, M. E. Nasir, W. Dickson, G. A. Wurtz, A. V. Zayats, *Nat. Comm.* **2015**, *6*, 7757.
[20] A. K. Popov, M. I. Shalaev, S. A. Myslivets, V. V. Slabko, I. S. Nefedov, *Appl. Phys. A* **2012**, *109*, 835.
[21] A. K. Popov, I. S. Nefedov, S. A. Myslivets, *ACS Photonics* **2017**, *4*, 1240.
[22] P. Segovia, G. Marino, A. V. Krasavin, N. Olivier, G. A. Wurtz, P. A. Belov, P. Ginzburg, A. V. Zayats, *Opt. Exp.* **2015**, *23*, 30730.
[23] J. Elser, R. Wangberg, V. A. Podolskiy, E. E. Narimanov, *Appl. Phys. Lett.* **2006**, *89*, 261102.
[24] P. B. Johnson, R.-W. Christy, *Phy. Rev. B* **1972**, *6*, 4370.
[25] S. Peruch, A. Neira, G. A. Wurtz, B. Wells, V. A. Podolskiy, A. V. Zayats, *Adv. Opt. Mat.* **2017**, *5*, 1700299.
[26] N. Bloembergen, R. K. Chang, S. Jha, C. Lee, *Phys. Rev.* **1968**, *174*, 813.
[27] A. Benedetti, M. Centini, C. Sibilia, M. Bertolotti, *J. Opt. Soc. Amer. B* **2010**, *27*, 408.
[28] M. Scalora, M. A. Vincenti, D. de Ceglia, V. Roppo, M. Centini, N. Akozbek, M. J. Bloemer, *Phys. Rev. A* **2010**, *82*, 043828.
[29] Y. Zeng, W. Hoyer, J. Liu, S. W. Koch, J. V. Moloney, *Phy. Rev. B* **2009**, *79*, 235109.
[30] P. Ginzburg, A. V. Krasavin, G. A. Wurtz, A. V. Zayats, *ACS Photonics* **2014**, *2*, 8.
[31] F. X. Wang, F. J. Rodríguez, W. M. Albers, R. Ahorinta, J. E. Sipe, M. Kauranen, *Phy. Rev. B* **2009**, *80*, 233402.
[32] J. Berthelot, G. Bachelier, M. Song, P. Rai, G. C. Des Francs, A. Dereux, A. Bouhelier, *Opt. Exp.* **2012**, *20*, 10498.
[33] C. Forestiere, A. Capretti, G. Miano, *J. Opt. Soc. Amer. B* **2013**, *30*, 2355.
[34] T. Stefaniuk, N. Olivier, A. Belardini, C. P. T. McPolin, C. Sibilia, A. A. Wronkowska, A. Wronkowski, T. Szoplik, A. V. Zayats, *Adv. Opt. Mat.* **2017**, *5*, 1700753.
[35] N. Bloembergen, R. K. Chang, C. H. Lee, *Phys. Rev. Lett.* **1966**, *16*, 986.
[36] M. McMahon, R. Lopez, R. Haglund, Jr., E. Ray, P. Bunton, *Phy. Rev. B* **2006**, *73*, 041401.

[37] C. Hubert, L. Billot, P. M. Adam, R. Bachelot, P. Royer, J. Grand, D. Gindre, K. D. Dorkenoo, A. Fort, *Appl. Phys. Lett.* **2007**, *90*, 181105.
[38] I. I. Smolyaninov, A. V. Zayats, C. C. Davis, *Phy. Rev. B* **1997**, *56*, 9290.
[39] L. Carletti, D. Rocco, A. Locatelli, C. De Angelis, V. Gili, M. Ravaro, I. Favero, G. Leo, M. Finazzi, L. Ghirardini, M. Celebrano, G. Marino, A. V. Zayats, *Nanotechnology* **2017**, *28*, 114005.
[40] D. E. Zelmon, D. L. Small, D. Jundt, *J. Opt. Soc. Amer. B* **1997**, *14*, 3319.
[41] D. N. Nikogosyan, *Nonlinear Optical Crystals: a Complete Survey*, New York, NY: Springer Science & Business Media, **2006**.
[42] Z. Knittl, *Optics of Thin Films: an Optical Multilayer Theory*, New York, NY: John Wiley & Sons, **1976**.